Semester Thesis

A tunable 20 GHz transmon qubit in a 3D cavity

Stefanie Miller

Supervisor: Dr. Sébastien Garcia

Principal Investigator: Prof. Dr. Andreas Wallraff

Quantum Device Lab
Laboratory for Solid State Physics
Swiss Federal Institute of Technology Zurich

Zurich, June 25, 2018

Abstract

Superconducting qubits are efficient realizations of quantum bits. They can be implemented and addressed in a 3D cavity with frequency ranges that are usually around $5-7$ GHz. A frequency tunable transmon qubit around 20 GHz together with a matching 3D cavity made of oxygen-free copper are designed in this thesis. This qubit-cavity system is then placed in a dilution fridge and measured. The mode splitting of the qubit-cavity system and the periodic tuning of the transmon through an external coil could be observed in the experiments. Time resolved measurements revealed qubit lifetimes of $T_1 \simeq 2$ µs and coherence times of $T_2^* \simeq 2$ µs using a Ramsey measurement $T_2 \simeq 3-4$ µs by spin-echo measurement.

Contents

1 Introduction

The experiment aims to realize and control the quantum mechanical form of a classical bit. Whereas the classical bit can be in either 0 or 1 state, the qubit, i.e. quantum bit, is described by $|\psi\rangle = \alpha\,|0\rangle + \beta\,|1\rangle$ with $|\alpha|^2 + |\beta|^2 = 1$.

Such qubits can be realized by superconducting circuits, which consists of capacitors, inductors and Josephson junctions [1]. The description of such a system is given by the quantization of an equivalent electronic circuit which is the basis for circuit quantum electrodynamics (circuit QED) [2]. In our experiment a qubit is realized by a transmon qubit that is placed inside a 3D cavity, where the two-level system interacts with an microwave cavity field.

The system of the cavity and the qubit is schematically depicted in figure 1 and described by the Jaynes-Cummings-Hamiltonian [3]

$$H_{JC} = \underbrace{\hbar\omega_\mathrm{q}\left(a^\dagger a + \frac{1}{2}\right)}_{\text{Electromagnetic field}} + \underbrace{\frac{\hbar\omega_\mathrm{r}}{2}\sigma^z}_{\text{Qubit}} + \underbrace{\hbar g(a^\dagger\sigma^- + a\sigma^+)}_{\text{Interaction}} + H_\kappa + H_\gamma. \tag{1}$$

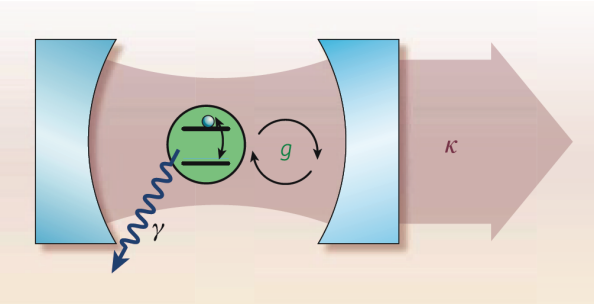

Figure 1: Schematical description of the cavity-qubit system. The purple color describes the electromagnetic field, the qubit state is colored in green. The interaction between cavity and qubit is indicated by the coupling constant g. The decay of the photon and the qubit, are denoted with the letters κ and γ, respectively. Taken from [4].

The first term corresponds to the electromagnetic field in the resonator which is a one-photon field in our experiment. The frequency ω_r denotes the resonance frequency of the cavity. It is assumed that the qubit can be modelled as a two-level system (second term), where ω_q denotes the transition frequency between the qubit states. The third term corresponds to the interaction between the cavity and the qubit and is described by the coupling constant g. The interaction term shows that we can either have a photon and the qubit in the ground state or the energy of the photon is transferred to the qubit and the qubit is then in the excited state. H_κ denotes the decay of the photon and H_γ describes the decay of the excited qubit caused by coupling to other modes or due to impurities in the superconductor, adsorption by the chip and others.

Neglecting the decay expressions in the Hamiltonian, we can find the excited eigenstates (dressed states) and eigenenergies [3]

$$|n,+\rangle = \sin(\theta_n)\,|n+1,\uparrow\rangle + \cos(\theta_n)\,|n,\downarrow\rangle \tag{2}$$

$$|n,-\rangle = \cos(\theta_n)\,|n+1,\uparrow\rangle - \sin(\theta_n)\,|n,\downarrow\rangle \tag{3}$$

$$E_{\pm,n} = \hbar\omega_r\,(n+1) \pm \frac{\hbar}{2}\sqrt{4g^2(n+1)+\Delta^2}. \tag{4}$$

Here, $|\uparrow\rangle$ ($|\downarrow\rangle$) denotes the ground (excited) state of the qubit. The angle θ_n is given by $\tan(2\theta_n) = \frac{2g\sqrt{n+1}}{\Delta}$ and $\Delta = \omega_\mathrm{q} - \omega_r$. The energy of the ground state is given by $E_{\uparrow,0} = -\frac{\hbar\Delta}{2}$. These eigenenergies lead to the spectrum with two specifically interesting regimes around $\Delta \approx 0$ called zero detuning and $g/\Delta \ll 1$ called dispersive regime.

In this first case, the qubit and the cavity are on resonance. Looking at the eigenenergies, we can find that there is a difference of

$$\delta E := E_{+,n} - E_{-,n} = 2\hbar g\sqrt{n+1}. \tag{5}$$

So, the difference of the two energies can be used to compute the coupling g.

In the limit of large detuning, $g/\Delta \ll 1$, we can apply the unitary transformation $U = \exp\left[\frac{g}{\Delta}(a\sigma^+ - a^\dagger\sigma^-)\right]$ and get [3]

$$UHU^\dagger \approx \hbar\left[\omega_r + \frac{g^2}{\Delta}\sigma^z\right]a^\dagger a + \frac{\hbar}{2}\left[\Omega + \frac{g^2}{\Delta}\right]\sigma^z. \tag{6}$$

One can observe that the cavity resonance frequency is shifted by $\pm g^2/\Delta$ depending on qubit state. This effect can be used for readout of the qubit.

Transition frequencies of the qubits are typically around $\sim 5-7$ GHz, e.g. in [5]. In this thesis, the goal is to investigate a new frequency regime for the qubit that is around ~ 20 GHz. More precisely, we are interested in the scaling of the transmon properties around this frequency. The work of the thesis includes the design of the cavity which is described in section 2, the design of the transmon qubit that is covered in section 3. An overview of the measurements and the setup can be found in section 4. The results of the measurements and its analysis are given in section 5.

2 Cavity Design and First Analysis

In this section the design of the cavity is described. Difficulties and changes of design compared to other 3D cavities at a frequency of ~ 7 GHz, are described. In the second part, the measurement and analysis of the produced cavity are presented.

2.1 Cavity Design

The transmon qubit will be placed in a resonator. A resonator is used to enhance the coupling of the qubit to a microwave field mode and can be used for readout [6]. In our experiment we consider a 3D cavity with conducting walls that is made out of oxygen-free copper. The inside of the cavity is vacuum, except for the transmon chip that is placed inside the cavity. As copper is a non-superconducting material is allows us to apply a magnetic field inside the cavity in order to change the transmon qubit frequency, see section 3.1.

The dimensions of the 3D cavity define the eigenfrequencies which can be computed based on the model of a rectangular waveguide and terminating both sides as

$$f_{lmn} = \frac{c}{2\pi\sqrt{\mu_R \cdot \epsilon_R}} \sqrt{\left(\frac{\pi \cdot l}{a}\right)^2 + \left(\frac{\pi \cdot m}{b}\right)^2 + \left(\frac{\pi \cdot n}{d}\right)^2} \tag{7}$$

where c denotes the speed of light in vacuum, μ_R the relative magnetic permeability and ϵ_R the relative permittivity of the material inside the cavity, a, b and c are the dimensions of the cavity, and l, m and n are integers. A derivation of equation 7 can be found in [7].

Equation 7 was used to get an idea of the dimensions using $\epsilon_r = 1$ assuming only vacuum as the filling material of the cavity. The first eigenfrequency was targeted to be ~ 20 GHz and the second one above ~ 25 GHz to ensure that it will not influence our measurements. A first estimation lead to the dimensions $x = 13$ mm, $y = 5$ mm and $z = 9$ mm. The cavity was drawn in CAD based on the standard cavity design from the group using the programme *Autodesk Inventor*. An example CAD drawing of the cavity can be seen in figure 2. The CAD drawing of the cavity together with the chip was then exported and used as a basis for the electric field simulation with *Ansoft HFSS*. The simulation was conducted by applying excitations to the two ports of the cavity in a frequency range between 15 GHz to 35 GHz.

The standard cavity design has a rounding of the edges of the rectangle in the xy-plane due to limits in machining. In the design process the radius of these edges were adjusted from 2.5 mm to 1 mm to receive a better rectangular cavity, thus closer to the analytically solvable cavity. The chip dimension in x-direction was reduced from 4.3 mm to 2 mm in order to have higher eigenfrequencies while keeping the same dimensions. Also, the typically used connectors were changed to a clamped wire like the Rydberg project cavities since we are in a different frequency regime and more importantly, the standard connectors are too large for the small cavity.

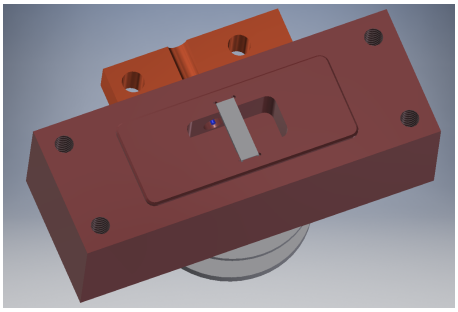

Figure 2: 3D drawing of the cavity (one half, purple) with a part of the pin clamp (red) and the chip (grey).

In an iterative process the cavity dimensions were adjusted based on the simulation and a subsequent simulation was conducted with the new design. Finally, the dimensions of the parameters were chosen as $x = 10$ mm, $y = 5$ mm and $z = 8$mm. For this design the first frequency at resonance is predicted by the simulation to be $f_0 = 19.88$ GHz.

2.2 Analysis of the Produced Cavity

After machining of the cavity, it was assembled together by brass screws which makes sure that the cavity is hold tight also under cold temperature conditions. A Sapphire chip was placed inside the cavity which takes care of the influence of the transmon chip that we will use at a later stage of the experiment.

We measure the cavity at room temperature by connecting the ports of the cavity to the vector network analyzer (VNA) (*Rohde & Schwarz*). A TOSM (Through - Open - Short - Match) calibration has to be conducted in the desired frequency range. Using the VNA leads to an analysis of the scattering matrix consisting of the S-parameters S_{ij} depending on the ports i, j of the cavity [7]. More precisely, S_{21} is the transmission of port 1 to port 2 and S_{11} the reflection on port 1.

We use these parameters to find the resonant frequencies of the cavity. In figure 3, the S_{21}-parameter, i.e. the transmission, is depicted for a long frequency range both from the simulation as well as the measurements. The simulation predicted the first resonance frequency at $f_1 \simeq 19.9$ GHz, $f_2 \simeq 33.3$ GHz, $f_3 \simeq 34.5$ GHz and $f_4 \simeq 35.5$ GHz. The resonance frequency were measured at $f_1 \simeq 20.1$ GHz, $f_2 \simeq 33.3$ GHz, $f_3 \simeq 34.5$ GHz and $f_4 \simeq 35.8$ GHz. All resonant frequencies can be observed very clearly except for the second one. The simulated and measured resonant frequencies differ by maximally ≈ 300 MHz.

To get more information about the cavity, its internal and external losses we have to look at the resonant frequency more carefully. The losses can be obtained by the S

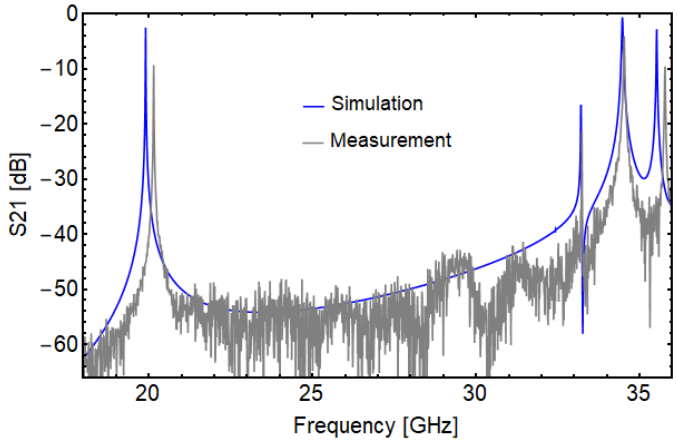

Figure 3: Simulated and measured transmission coefficient as a function of frequency. The measurement was conducted at room temperature.

parameters which are given by the equations

$$|S_{11}|^2 = 1 - \frac{4\kappa_1(\kappa_2 + \kappa_{int})}{\kappa_{tot}^2 + 4(\omega - \omega_0)^2}, \tag{8}$$

$$|S_{22}|^2 = 1 - \frac{4\kappa_2(\kappa_1 + \kappa_{int})}{\kappa_{tot}^2 + 4(\omega - \omega_0)^2}, \tag{9}$$

$$|S_{21}|^2 = \frac{4\kappa_2\kappa_1}{\kappa_{tot}^2 + 4(\omega - \omega_0)^2}, \tag{10}$$

where κ is the loss rate of a resonant photon in the cavity which describes the width of the resonant frequency ω_0. The total losses $\kappa_{tot} = \kappa_{int} + \kappa_{ext}$ are given by the internal and external losses, $\kappa_{ext} = \kappa_1 + \kappa_2$ with κ_1 and κ_2 corresponding to the two ports of the cavity, respectively. The equations can be obtained by extending the theory in [8] to a two port cavity.

Figure 4 shows the results of the transmission and reflection measurement at room temperature. The modulus of the different S parameters are plotted in an logarithmic scale. The resonance frequency is found to be $f_0 \simeq 20.13$ GHz which is close to the value from the simulation. The internal losses of the cavity are given by $\kappa_{int}/2\pi \simeq 3.9$ MHz. The internal losses of the cavity can be reduced by cleaning the cavity with citric acid. The internal quality factor is given by $Q_{int} = \frac{f_0}{\kappa_{int}} \simeq 5 \cdot 10^3$ at room temperature. The input (1) and output (2) coupling microwave antennas are placed asymmetrically with $\kappa_1/2\pi \simeq 0.98$ MHz and $\kappa_2/2\pi \simeq 2.0$ MHz. This arrangement is based on reducing the amount of reflection on the ports. Here, we limit the losses at port 2 by the expected value of κ_{int} at cryogenic temperatures and using the relation $\kappa_2 \simeq \kappa_{int} \simeq 2\kappa_1$, we can reduce the reflection on port 1 to ≈ 20 % on resonance. The external quality factor is then given by $Q_{ext} \simeq 6.7 \cdot 10^3$ at room temperature. The variables A_1 and A_2 account for small offsets of the reflection parameter of port 1 and 2, respectively.

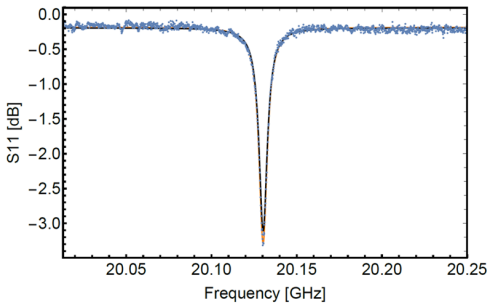

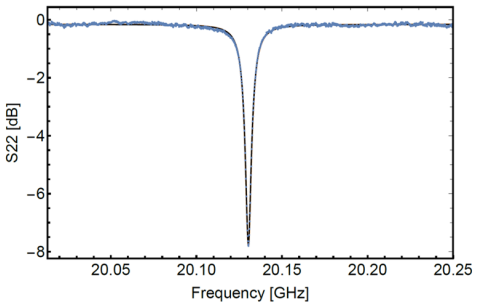

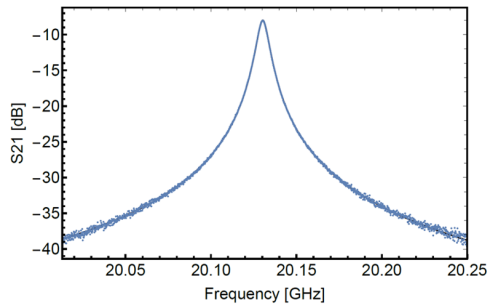

	Estimate	Standard Error	Confidence Interval
f0	20.1303	7.27829×10^{-6}	{20.1303, 20.1304}
$\kappa 1$	0.983863	0.00315291	{0.977682, 0.990044}
$\kappa 2$	2.01001	0.00633627	{1.99759, 2.02244}
κint	3.91325	0.0151965	{3.88346, 3.94304}
A1	−0.193465	0.00348258	{−0.200293, −0.186638}
A2	−0.160569	0.00355825	{−0.167545, −0.153593}

Figure 4: Transmission and reflection measurements of the first cavity mode at room temperature. Each S-parameter is individually fitted, in orange, and all S-parameters are fitted together, in black. The fitted parameter results are presented in the table.

The measurements were repeated for different cavity orientations as well as removing the pins from the cavity and putting them back by removing the pin clamp, see figure 5. The pinclamp design was necessary due to the limited space on this particular cavity.

We found that the cavity allows for good reproduction of the measurements. In an iterative process, the microwave antennas were removed from the cavity and then put back inside the cavity, while keeping the setup of the pins fixed. The measurement in figure 6 shows that the different cavity losses in each step of the iteration change by maximally 5 %. This reproduction behaviour is essential since we have to replace the Sapphire chip with the Transmon chip by removing the pin clamp of the cavity.

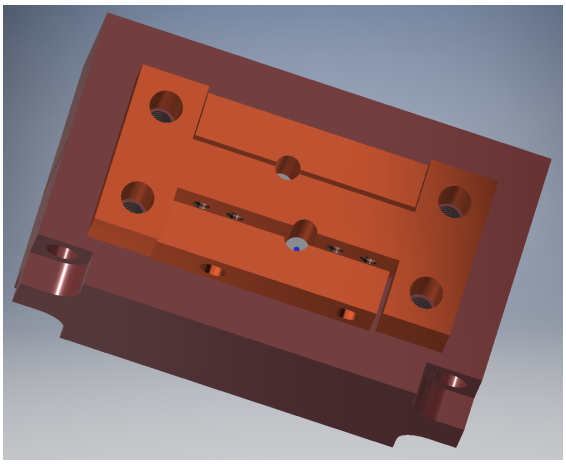

Figure 5: 3D drawing of the cavity (dark red) with the pin clamp constituents (red). The pin clamp consists of one H-shaped part, which is fixed onto the cavity, and two smaller parts that clamp each of the wire connectors.

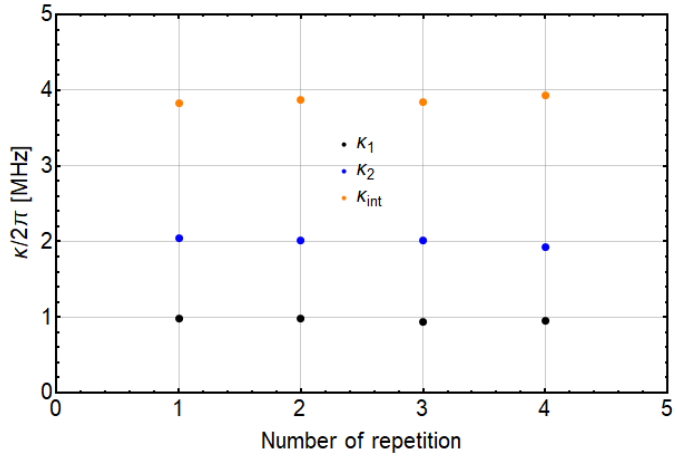

Figure 6: Reproduction measurement. In each iteration the microwave antennas were removed from the cavity and then put back inside the cavity. The measurement shows the changes in the internal losses κ_{int} and external losses κ_1 and κ_2.

3 Transmon Design

In this section we present the design of the transmon chip. Difficulties and changes of design compared to other transmons are discussed. First, the physics of a Transmon qubit is briefly discussed, then the design process is described.

3.1 Transmon qubit Hamiltonian

At first, one could assume that a qubit can be realized by a quantized LC-oscillator. However, rather than having two distinct energy states, that we want to denote with $|0\rangle$ and $|1\rangle$, the harmonicity of this system leads to many energy states with the same energy difference which makes it difficult to work with two energy states only. Therefore, an anharmonicity needs to be introduced that helps to work with selected energy states. [1].

In our experiment the qubit is realized by a LC-circuit with a superconducting material. A Josephson junction consists of two superconducting electrodes which are separated by a thin insulating layer, see figure 7, which is used as a non-linear inductance that satisfies the anharmonicity requirements at low temperature [1].

The effective Hamiltonian of the Transmon system reads [9]

$$H = 4E_C(\hat{n} - n_g)^2 - E_J \cos\hat{\varphi}, \tag{11}$$

where n_g is the effective charge offset, the quantum mechanical operator $\hat{n}$ denotes the charge number, i.e. the number of Cooper pairs difference between the two electrodes, and $\hat{\varphi}$ denotes the phase difference of the two superconductors. $E_C = \frac{e^2}{2C_\Sigma}$ denotes the

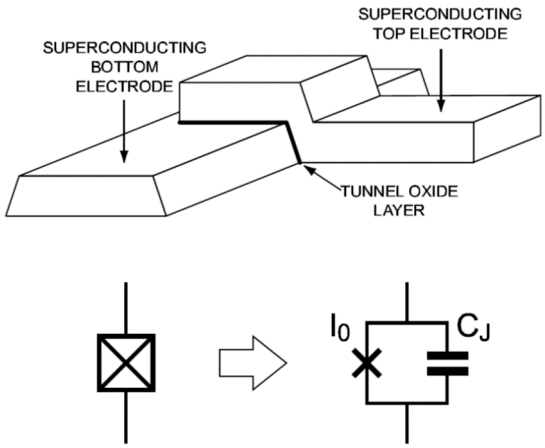

Figure 7: Top: Schematic of a Josephson junction which consists of two superconducting electrodes that are separated by a tunnel oxide layer. Bottom: Josephson junction model with an irreducible Josephson circuit element in parallel to a parallel plate capacitance formed by the two electrodes. Taken from [1].

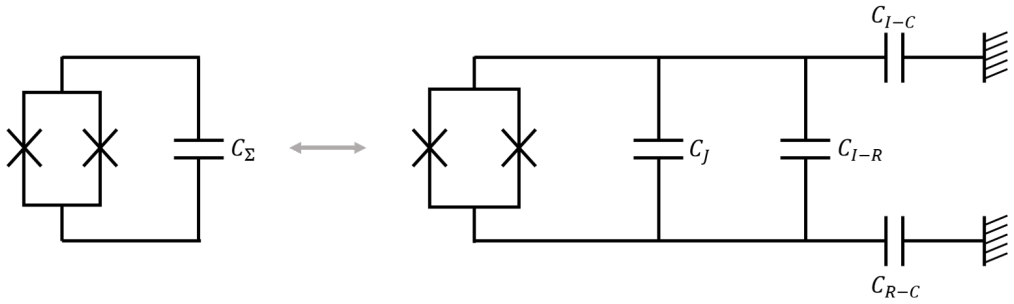

Figure 8: Drawing of the circuit in a summarized (left) and a detailed version (right). The equivalent capacitance C_Σ is given by the junction capacitance C_J, the capacitance between the two pads of the transmon (island and reservoir) C_{I-R} and the capacitance between each of the pads and the cavity C_{I-C} and C_{R-C}.

charging energy where C_Σ is the equivalent capacitance which is given by

$$C_\Sigma = C_J + C_{I-R} + \frac{1}{\frac{1}{C_{I-C}} + \frac{1}{C_{R-C}}}, \tag{12}$$

where C_J is the junction capacitance, C_{I-R} is the capacitance between the two pads of the transmon and C_{I-C} and C_{R-C} respectively, denote the capacitance between each of the pads and the cavity, see figure 8. E_J is the Josephson energy.

In this setup we work with a two Josephson junction in parallel which is known as a superconducting quantum device loop (SQUID loop) which allows for qubit frequency tuning. The flux through this loop can be adjusted by a magnetic field which makes the Josephson energy $E_J(\Phi_{ext}) = E_J \cos(\pi\Phi_{ext}/\Phi_0)$ adjustable [1]. It is dependent on the external magnetic flux Φ_{ext} which can be varied by applying a magnetic field that penetrates the SQUID loop. The magnetic field can be obtained by an external coil.

The transmon is operated in the regime $E_J/E_C \gtrsim 50$, where the influence of the charge noise on the energy levels is low [9]. In this limit, the eigenenergies E_m, $m \geq 0$, are given by [9]

$$E_m \simeq -E_J + \sqrt{8E_C E_J}(m + 1/2) - \frac{E_C}{12}(6m^2 + 6m + 3). \tag{13}$$

3.2 Transmon-cavity coupling

We need to calculate the coupling constant g. For this we will start by deriving the classical interaction Hamiltonian and then quantize it. Consider an electric field $\vec{E}_0$ oriented parallel to the pads as depicted in figure 9. The corresponding electric potential is given by $V_0(\vec{r}) = -E_{\text{cav}} \cdot x$. The charges on the pads are taken as $Q = Q_1 = -Q_2$ due to the symmetry of the system and their corresponding distribution by $\rho(\vec{r}) = \rho_1(\vec{r}) + \rho_2(\vec{r})$. The interaction Hamiltonian is then given by the interaction of the charges with the

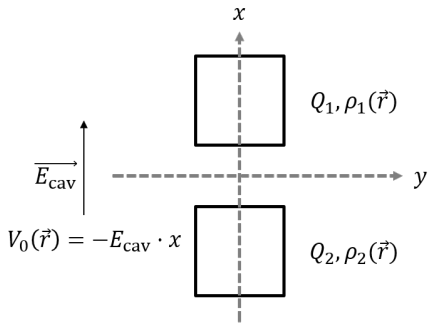

Figure 9: Schematic of the transmon exposed to an electric field.

electric field

$$H = \int \rho(\vec{r}) V_0(\vec{r}) \mathrm{d}\vec{r} = -E_{\text{cav}} Q d_{\text{eff}},$$

where we introduced the effective distance between the pads given by

$$d_{\text{eff}} = \int \rho_N(\vec{r}) \cdot x \; d\vec{r}, \quad \text{where } \rho_N(\vec{r}) = \frac{\rho_1(\vec{r})}{|Q|} + \frac{\rho_2(\vec{r})}{|Q|}. \tag{14}$$

This computation was realized with the software *Ansoft Maxwell* using *Qsurf* for the surfaces of the island and the reservoir. For simplification only the large surfaces (in the xy-planes) were taken into account.

Unfortunately, we could not find a way to directly export the effective distance while doing an optimetric analysis. In [10], *VBA programming* was used to automatically get the result. In that work, it was found that the effective distance approaches the geometrical distance between the center of the two pads for bigger separations between them whereas for smaller distances it was found to be smaller. Due to moderate gain of knowledge on one side and large time investment on the other side, the effective distance was computed by approximating the charge distribution uniformly on the pads rather than explicitly computing the effective distance for each of the possible Transmon designs using the charge surface simulation.

So far we have only considered the effective distance with respect to the geometric capacitance. However, we have the junction capacitance and the geometric capacitance in parallel in our system, therefore, $Q_J = C_J V$ and $Q_{\text{geo}} = C_{\text{geo}} V$. Thus, the effective distance is given by

$$d_{\text{eff}} = \frac{Q_J \cdot d_{\text{eff,J}} + Q_{\text{geo}} \cdot d_{\text{eff,geo}}}{Q_J + Q_{\text{geo}}} \simeq d_{\text{eff,geo}} \frac{C_{\text{geo}}}{C_J + C_{\text{geo}}} \tag{15}$$

This effect was forgotten in the original design. It will lead to a reduced coupling constant.

Now we go to the quantization. The electric field can be written as $\hat{E} = E_0\ (\hat{a}^\dagger + \hat{a})$, where $E_0 = \sqrt{\frac{\hbar\omega_r}{2\varepsilon_0 V}}$ with V being the mode volume. For the charge we write $\hat{Q} = -2e\ \hat{n}$. Then we can consider the interaction part of the Hamiltonian to find

$$H_{\text{int}} = -E_{\text{cav}}\ Q\ d_{\text{eff}} = 2e\ \hat{n}\ d_{\text{eff}}\ E_0(\hat{a}^\dagger + \hat{a})$$
$$H_{\text{int,JC}} = \hbar g\ (a^\dagger\sigma^- + a\sigma^+)$$

Using $\sigma^+ = |e\rangle\langle g|$ and $\sigma^- = |g\rangle\langle e|$ we compute $\langle e|\, H_{\text{int}}\, |g\rangle$ for both representations and find [9]

$$\hbar g_{eg} = 2eE_0 d_{\text{eff}} \langle e|\, \hat{n}\, |g\rangle \simeq 2e\ E_0\ d_{\text{eff}} \frac{1}{\sqrt{2}} \left(\frac{E_J}{8E_C}\right)^{1/4}. \tag{16}$$

The mode volume $V = \frac{\int \varepsilon_r(\vec{r})||\vec{E}(\vec{r})||^2 \mathrm{d}\vec{r}}{\max(||\vec{E}(\vec{r})||^2)}$ of the cavity, where $\vec{E}(\vec{r})$ describes the electric field and ϵ_r the permittivity, describes the volume of mode inside the cavity. Using an empty cavity for the computation gives a first estimation of the mode volume $V \approx 100$ mm^3. The presence of the chip was taken account of in the computation by analytically adding the permittivity in the numeric integration of the cavity field simulation with the chip inside of the cavity. In the simulation we deal with artefacts at the boundary of the cavity. In order to minimize these effects, we perform the simulation with different mesh sizes, vary the lengths in all directions by var and compare the ratios of the volumes $V_{-\text{var}}/V_{\text{full}}$ to the ratios of the lengths $1 - 2\text{var}/\text{L}$. It turned out that the best match is given by a mesh size of 0.2 mm where $V \approx 96.7$ mm^3. Here we used a variation in y-direction of var = 0.5 mm in the ratio perspective where the variation of the electric field due to artifacts is reduced.

3.3 Transmon Design Process

The transmon design is based on the typical design where two superconducting pads joined by a SQUID junction are placed on a Sapphire chip. The dimensions of the pads of the transmon as well as displacement between the pads lead to different capacitances, frequency ranges and other quantities of the qubit. In a first approach the pads were designed to be symmetric for simplification. Using the software *Ansoft Maxwell*, the capacitances of the pads as well as the capacitances between the pads and the cavity were computed for different pad dimensions and displacements between the pads. The simulation is based on the Optimetrics tool where voltage excitations for the cavity and the two pads were set. We present the used equations for our design in the following.

- The Josephson energy is given by $E_J = \frac{h\Delta_{SC}}{8e^2}\frac{2A_J}{R_{n,A_J}}$. Here, $\Delta_{SC} = 162$ µeV denotes the superconducting gap of the junction material and R_{n,A_J} denotes the surface normal resistance of the junction with $R_n = \frac{R_{n,A_J}}{2A_J}$. The formula can be derived using $E_J = \frac{\hbar I_c}{2e}$, where I_c is the critical current of the superconductor, and the Ambegaokar-Baratoff formula for tunnel junctions at $T = 0$ K, $I_c R_n = \pi\Delta_{SC}/2e$ [11].

- The junction capacitance is given by $C_J = 2C_{A_J}A_J$ where $C_{A_J} \simeq 60$ fF/µm^2 is the junction capacitance per area for typical Al−AlO_x−Al junctions produced in our lab. To receive a capacitance we have to multiply this by the area A_J of the junction. The multiplication by 2 arises from the fact that we have two junctions in parallel in the SQUID loop. The junction area A_J is defined by equation 17 such that we reach the desired qubit frequency. In our limit of $E_J \gg E_C$, we simplify the equation to $h \cdot f_{01} \simeq \sqrt{8E_J E_C}$. Using the expression for E_J and $E_C = \frac{e^2}{2C_\Sigma} = \frac{e^2}{2(C_{\Sigma_{geo}}+C_J)}$ together with the expression of the junction capacitance C_J, one can isolate the junction area and gets $A_J \simeq \frac{C_{\Sigma_{geo}}}{\frac{\Delta}{hf_{01}^2 R_{n,A_J}} - 2C_{A_J}}$.

- Compared to usual transmon designs with a frequency around ~ 7 GHz, we need to reach different values for the Josephson energy E_J and the charging energy E_C in order to reach a frequency of ~ 21 GHz. Based on equation 13, we have

$$h \cdot f_{01} = E_1 - E_0 \simeq -E_C + \sqrt{8E_J E_C}. \tag{17}$$

  As mentioned above, the transmon is operated in the regime $E_J/E_C \gtrsim 50$, so getting to the desired frequency essentially reduces to increase $E_J \cdot E_C$ by a factor of 9. We increase both energies by a factor of 3 to keep a similar ratio as in the cases of usual transmon designs. The needed junction energy is represented as function of the charging energy for different qubit frequencies on figure 10a along with the solutions provided with different the junction area. The points where the lines cross then define the solutions. One can clearly observe that decreasing the junction surface resistance (full vs. dashed lines) leads to a decrease of the needed junction energy. Figure 10b demonstrates that this solution also leads to smaller junction area.

- The dispersive shift is the frequency shift that the cavity frequency is shifted due to the cavity-qubit coupling, where we consider the two transition frequencies $f_{0\to1}$ and $f_{1\to2}$. $\alpha \approx E_C$ denotes the difference in the transition frequencies caused by the anharmonicity of the Josephson junction.

- The Purcell-limited lifetime $T_{\text{Purcell}} = 1/\Gamma_P$ corresponds to the spontaneous emission which is given by the rate $\Gamma_P = \frac{g^2}{\Delta^2}\kappa$, where g is the coupling strength of the resonator, Δ is the detuning of the qubit and resonator frequency and κ is the resonator dissipation rate. This relation is only valid in the dispersive limit.

- The coupling constant g needs to be sufficiently high such that the dispersive shift is high enough so we can actually readout the qubit state as discussed in section 1. On the other hand, if it is chosen too large, we are no longer able to measure the intrinsic lifetime of the qubit but are limited by the Purcell-limited lifetime.

- The charge dispersion describes the variation of the energy levels of the Transmon with respect to environmental offset charges and gate voltage [9]. The equations for the charge dispersion as well as transmon dephasing time $T2_{\text{charge}}$ can be found in [9].

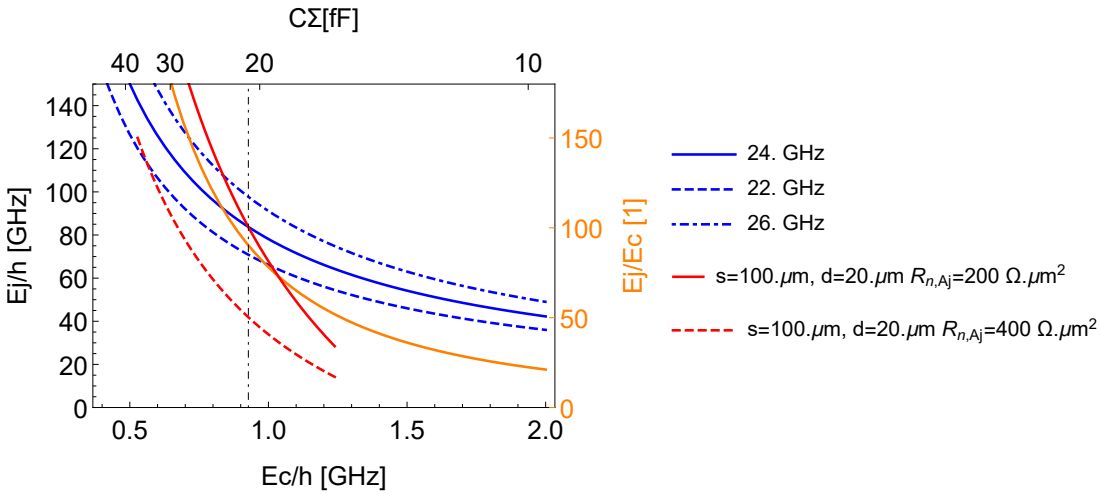

(a)

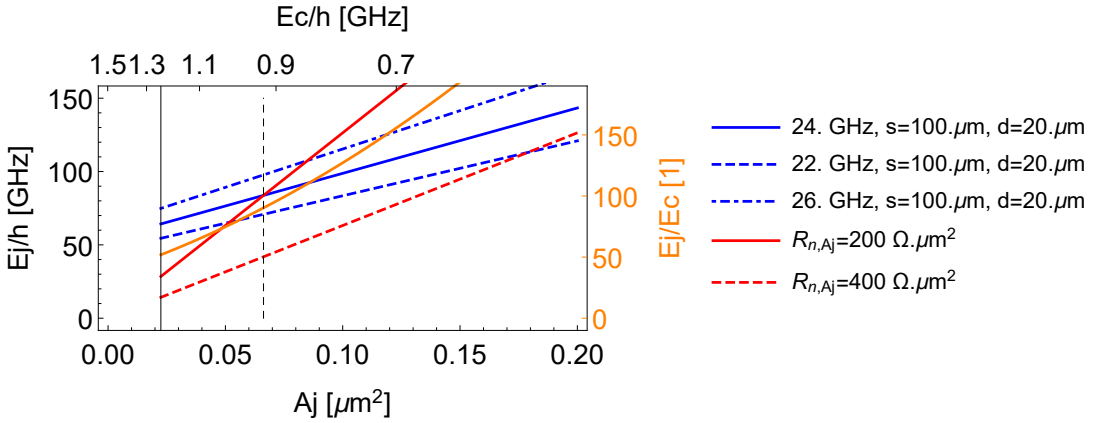

(b)

Figure 10: (a) Solution representation as function of charging energy. Needed junction energy for different frequencies in blue. Junction energy corresponding to charging energy for different transmon geometries and junction thicknesses (equivalent to surface normal resistance $R_{n;Aj}$) while varying junction area in red. Vertical line is showing the crossing of solutions that was used. The orange curve with corresponding right axis gives the ratio of junction and charging energy for a 24 GHz transmon. (b) Solution representation as a function of junction area (curves start at smallest achievable junction area by our fabrication). Needed junction energy for a given geometry with different frequencies in blue. Junction energy for different junction thicknesses which are equivalent to normal resistance times junction area $R_{n;Aj}$ in red. The orange curve with corresponding right axis gives the ratio of junction and charging energy for a 24 GHz transmon.

The used equations for the transmon design are summarized in table 1.

Quantity	**Equation**
Josephson energy	$E_J = \frac{h\Delta_{SC}}{8e^2}\frac{2A_J}{R_{n,A_J}}$
Junction capacitance	$C_J = 2C_{A_J}A_J$
Junction area	$A_J \simeq \frac{C_{\Sigma_{geo}}}{\frac{\Delta}{hf_{01}^2 R_{n,A_J}} - 2C_{A_J}}$
Qubit frequency	$h \cdot f_{01} = E_1 - E_0 \simeq -E_C + \sqrt{8E_J E_C}$
Coupling constant	$g = \frac{2e}{\sqrt{2}\hbar}\left(\frac{E_J}{8E_C}\right)^{1/4} d_{\text{eff}} E_0$
Dispersive shift	$\chi = g^2\left(\frac{1}{\omega_{01}-\omega_r} - \frac{1}{(\omega_{01}-\alpha)-\omega_r}\right)$
Purcell-limited lifetime	$T_{\text{Purcell1}} = \frac{\Delta^2}{\kappa g^2}$
Charge dispersion	$\varepsilon_{\text{charge}} = \frac{2}{\pi}\left(\frac{E_J}{2E_C}\right)^{5/4}\exp\left(-\sqrt{\frac{8E_J}{E_C}}\right)$
$T2_{\text{charge}}$	$T2_{\text{charge}} = \frac{\hbar}{A\pi\varepsilon_{\text{charge}}}$

Table 1: Equations for the calculated quantities that were used to determine the Transmon design.

Due to a rather high coupling and low Purcell-limited lifetime, the pads were designed to be asymmetric in a new approach. The dimension parallel to the connection of the two pads was fixed while the other dimension as well as the displacement between the pads were varied in the simulation. The final chip design is shown in figure 11. The calculations for characteristic values such as the coupling constant or Purcell-limited lifetime for different transmon designs are stated in figure 12.

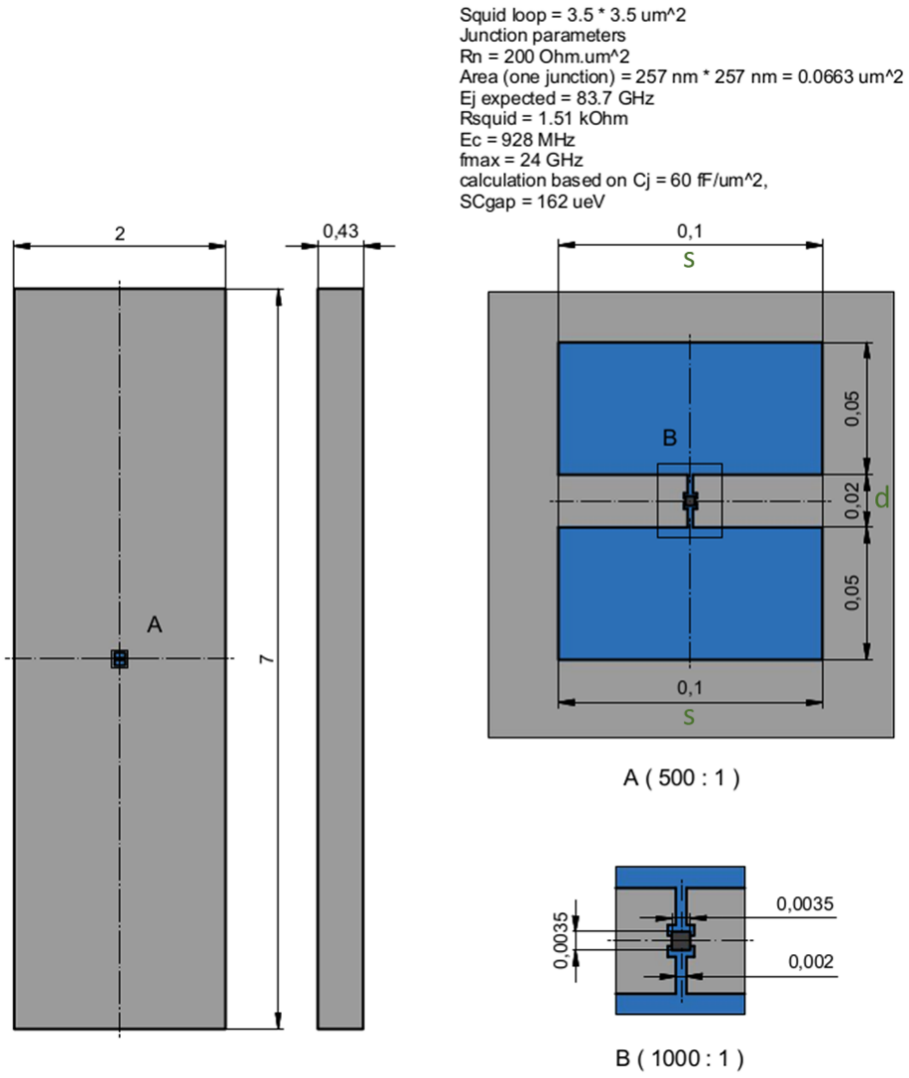

Figure 11: Final chip design. The green letters show the parameters based on which the computations of the quantities in figure 12 were computed.

Pad size x [μm]	Pad size y [μm]	Pad dist. y [μm]	$C_{Is1\text{-}Cav}$ [fF]	$C_{Res\text{-}Cav}$ [fF]	$C_{Is1\text{-}Res}$ [fF]	Aj [μm^2]	$\sqrt{Aj}$ [μm]	Cj squid [fF]	Cj/CΣ	Ec [GHz]	Ej [GHz]	g [MHz]	$T1_{Purcell}$ [μs]	χ [MHz]	Ej /Ec	ϵ_{charge} [MHz]	$T2_{charge}$ [us]
50.	50.	20.	8.01	7.99	4.01	0.0439	0.21	5.27	0.397	1.46	55.5	97.4	143.	−1.25	38.1	0.623	814.
50.	50.	30.	8.25	8.23	3.56	0.0425	0.206	5.1	0.399	1.52	53.7	109.	114.	−1.67	35.4	1.1	461.
50.	50.	40.	8.47	8.44	3.28	0.0417	0.204	5.	0.4	1.55	52.7	121.	92.6	−2.13	34.	1.49	341.
50.	50.	50.	8.67	8.65	3.09	0.0413	0.203	4.96	0.4	1.57	52.2	133.	76.2	−2.63	33.3	1.74	292.
75.	50.	20.	9.45	9.42	5.78	0.0552	0.235	6.62	0.387	1.13	69.8	110.	112.	−1.11	61.6	0.00761	66600.
75.	50.	30.	9.71	9.69	5.07	0.0526	0.229	6.31	0.389	1.19	66.5	122.	90.6	−1.47	55.7	0.0212	23800.
75.	50.	40.	9.95	9.92	4.62	0.0511	0.226	6.13	0.39	1.23	64.6	135.	74.	−1.89	52.4	0.0381	13300.
75.	50.	50.	10.2	10.1	4.31	0.0502	0.224	6.02	0.391	1.26	63.4	149.	61.4	−2.35	50.4	0.0551	9200.
100.	50.	20.	10.7	10.7	7.59	0.0663	0.257	7.95	0.381	0.928	83.7	121.	92.4	−1.03	90.3	0.0000945	5.36×10^{6}
100.	50.	30.	11.	11.	6.63	0.0626	0.25	7.51	0.383	0.987	79.1	134.	75.3	−1.37	80.1	0.000413	1.23×10^{6}
100.	50.	40.	11.3	11.2	6.01	0.0603	0.246	7.24	0.384	1.03	76.3	148.	61.9	−1.76	74.3	0.000995	509000.
100.	50.	50.	11.5	11.4	5.57	0.0589	0.243	7.06	0.385	1.05	74.4	162.	51.6	−2.18	70.6	0.00178	284000.
125.	50.	20.	11.8	11.8	9.44	0.0773	0.278	9.27	0.376	0.786	97.6	131.	78.6	−0.983	124.	1.15×10^{-6}	4.4×10^{8}
125.	50.	30.	12.2	12.1	8.22	0.0724	0.269	8.69	0.378	0.843	91.5	145.	64.5	−1.31	109.	8.05×10^{-6}	6.29×10^{7}
125.	50.	40.	12.4	12.4	7.43	0.0694	0.264	8.33	0.379	0.882	87.8	159.	53.4	−1.67	99.6	0.0000264	1.92×10^{7}
125.	50.	50.	12.7	12.6	6.87	0.0675	0.26	8.1	0.38	0.909	85.3	174.	44.6	−2.08	93.8	0.0000579	8.75×10^{6}
150.	50.	20.	12.9	12.9	11.3	0.0882	0.297	10.6	0.373	0.683	111.	141.	68.5	−0.95	163.	1.4×10^{-8}	3.62×10^{10}
150.	50.	30.	13.2	13.2	9.86	0.0823	0.287	9.87	0.375	0.736	104.	155.	56.5	−1.26	141.	1.53×10^{-7}	3.31×10^{9}
150.	50.	40.	13.5	13.5	8.89	0.0785	0.28	9.42	0.376	0.773	99.2	170.	46.9	−1.61	128.	6.92×10^{-7}	7.32×10^{8}
150.	50.	50.	13.8	13.7	8.2	0.076	0.276	9.12	0.377	0.801	96.	186.	39.4	−2.01	120.	1.93×10^{-6}	2.63×10^{8}

Figure 12: Different solutions for different transmon geometries with a maximal frequency of 24 GHz with a junction normal area resistance $R_{n,A_J} = 200\ \Omega.\mu m^2$, with a 19.87 GHz resonator and 2 MHz cavity linewidth for the estimations of Purcell-limited lifetime and dispersive shift. The green background give the values of the designed transmon.

3.4 Produced Transmon

The produced transmon chip is shown in figure 13. The transmon chip is placed inside the cavity and is fixed by two small pieces of Indium on each of the two sides where the transmon is placed into, see figure 13a. It turned out that the designed chip was not producable because pads were designed too close to fabricate the junction. The residual exposure of the photoresist inbetween the pads was not sufficient to support the bridge for the junction. Therefore, the SQUID loop had to be placed outside of the two pads rather than inbetween as was designed, see figure 13b.

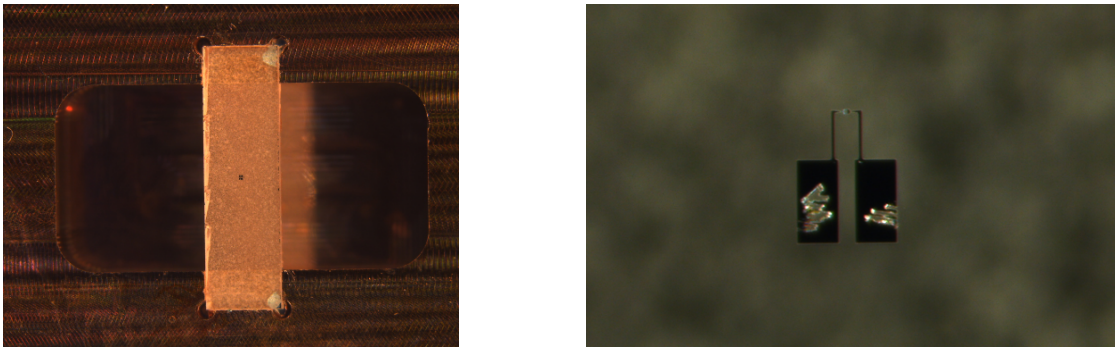

(a) (b)

Figure 13: Images of the transmon chip produced with fabrication number 180508 and probed normal resistance 1.43 kΩ.(a) Produced transmon chip placed inside the cavity. (b) Close-up of the produced transmon chip.

A follow-up simulation lead to slightly increased values of the capacitances, namely $C_{I-C} = C_{R-C} = 11.8$ fF rather than 10.7 fF and $C_{I-R} = 9.58$ fF rather than 7.59 fF. The charge distribution of the pads is depicted in figure 14.

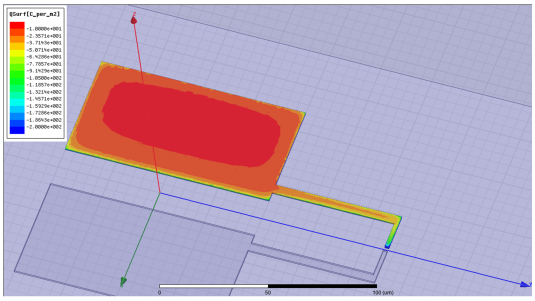

(a) Left top

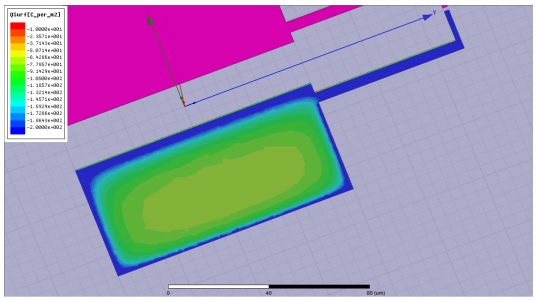

(b) Left bottom

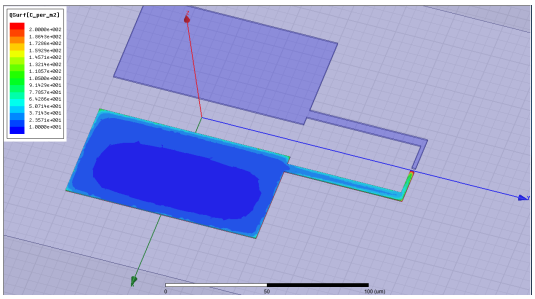

(c) Right top

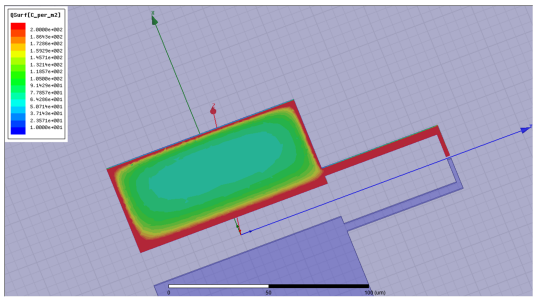

(d) Right bottom

Figure 14: Simulated charge distribution of the produced design. The left part in figure 13b is depicted in (a) top and (b) bottom. The right part is depicted in (c) top and (d) bottom.

4 Measurements

This section gives an overview of the conducted measurements with the qubit-cavity system. First, the theoretical background of the measurements will be outlined which summarizes the typical measurements conducted with a qubit-resonator system. Then, the measurement setup of the experiment is described.

4.1 Theoretical summary of measurements

4.1.1 Rabi oscillation

Consider two levels of an atom, i.e. the ground state $|g\rangle$ and the excited state $|e\rangle$. The atom may interact with light via the dipole interaction. Assuming the field to be $\vec{E}(t) = \hat{\epsilon}E_0\cos(\omega t)$ with an angular frequency of ω and $\hat{\epsilon}$ the unit polarization vector of the field. Then the Hamiltonian of this system is given by the atomic part and the interaction part $H_{int}(t) = -\vec{d}\cdot\vec{E}$ where $\vec{d}$ is the atomic dipole operator. The Rabi frequency is given by $\Omega = \frac{\langle g|\hat{\epsilon}\cdot\vec{d}|e\rangle E_0}{\hbar}$.

Let $|\Psi\rangle = c_g|g\rangle + c_e|e\rangle$ be the atomic state. Using the Schrödinger equation $i\hbar\partial_t|\Psi\rangle = H|\Psi\rangle$ and assuming that the atom is initially in the ground state we find

$$c_g(t) = \mathrm{e}^{\mathrm{i}\Delta \mathrm{t}/2}\left[\cos\left(\frac{1}{2}\tilde{\Omega}\mathrm{t}\right) - \mathrm{i}\frac{\Delta}{\tilde{\Omega}}\sin\left(\frac{1}{2}\tilde{\Omega}\mathrm{t}\right)\right] \tag{18}$$

$$c_e(t) = -i\mathrm{e}^{\mathrm{i}(\Delta \mathrm{t}/2-\omega \mathrm{t})}\frac{\Omega}{\tilde{\Omega}}\sin\left(\frac{1}{2}\tilde{\Omega}\mathrm{t}\right) \tag{19}$$

where $\tilde{\Omega} = \sqrt{\Omega^2 + \Delta^2}$ is the generalized Rabi frequency. The details of the derivation can be found in [12]. The modulus of these coefficients describe the occupation probability of the corresponding state. Using this, we can observe that the oscillations are dependent on either the time or the Rabi frequency which itself is dependent on the amplitude of the applied electric field. Therefore, Rabi osciallation can be performed when either the amplitude of the applied pulse E_0 or the length of the pulse t is varied.

The Rabi measurement is used to as a calibration measurement for the pulses that are applied in the measurements [13]. The measurements that are conducted are described in the following.

4.1.2 Energy-relaxation and coherence time

$\mathbf{T_1}$ measurement The energy-relaxation is a spontaneous decay which is related to the interaction of a quantum system with its environment. To determine the energy relaxation time T_1 the following experiment can be performed. A π-pulse is applied to the qubit, bringing the qubit into the excited state. After waiting for Δt, the qubit state is measured, see figure 15. Performing many such experiments with different time delays Δt leads to a characteristic exponential decay $\propto \mathrm{e}^{-\Delta \mathrm{t}/\mathrm{T}_1}$, from which T_1 can be extracted. [14].

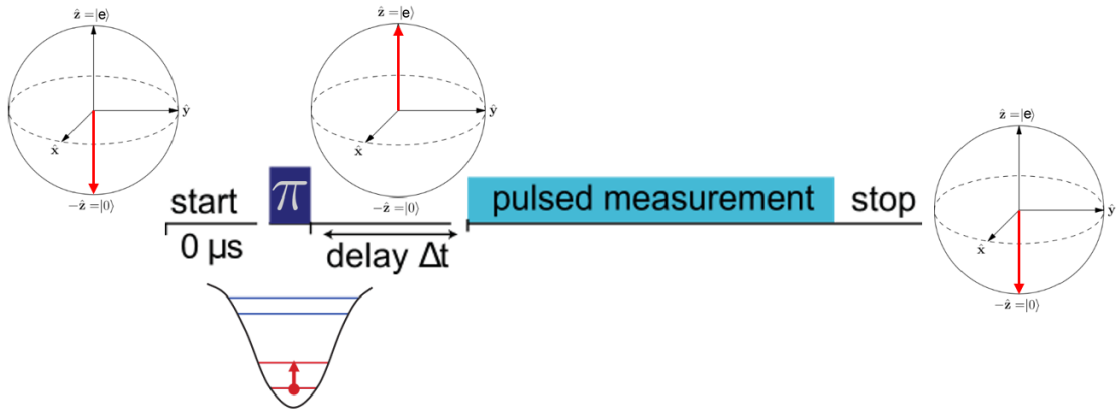

Figure 15: Measurement scheme for energy relaxation time T_1. Taken from [15].

Note that T_1 among others includes the spontaneous emission, whose rate is given by the Purcell rate $\Gamma_P = \frac{g^2}{\Delta^2}\kappa$, where g is the coupling strength of the resonator, Δ is the detuning of the qubit and resonator frequency and κ is the resonator dissipation rate.

Ramsey Measurement The phase decoherence time T_2^* relates to the energy decay rate $1/T_1$ and an additional decoherence rate arising from fluctuations of the qubit transition frequency, called pure dephasing [14]. The Ramsey experiment is an implementation of this measurement. The experiment starts with a $\pi/2$ rotation around the y-axis to bring the qubit to the x-axis in an equal superposition. After a free evolution time Δt a second $\pi/2$ rotation is performed around the y-axis, followed by the measurement of the qubit, see figure 16. Similarly to the energy-relaxation time, we can extract the decoherence

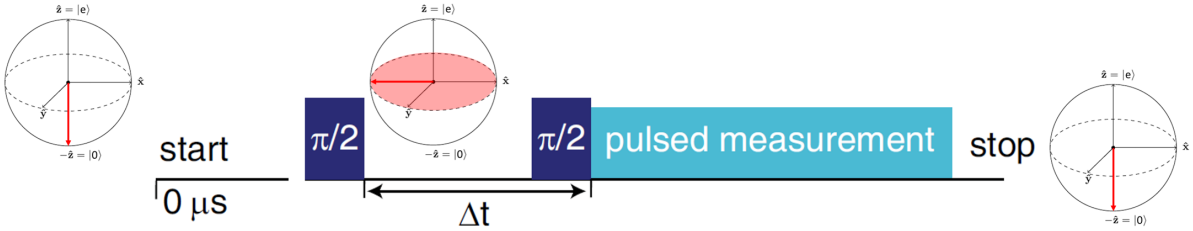

Figure 16: Measurement scheme for coherence time T_2^*. Modified after [14].

time by repeating the experiment which leads to an exponentially decaying envelope that is proportional to $e^{-\Delta t/T_2^*}$, where $\frac{1}{T_2^*} = \frac{1}{2T_1} + \frac{1}{T_\phi}$. The first term denotes the possibility of the qubit to make a transition from the excited to the ground state (or the other way round), the second term describes decays owing to random fluctuations in the precession

time that cause the different qubits to get out of phase with each other [16]. In our case, we do not consider many states at a single time which is the case for NMR, but average over many measurements of the single qubit. Thus, we consider temporal fluctuations rather than spatial fluctuations [16].

Spin-Echo Measurement Another measurement that can be performed is the spin-echo measurement [17]. Essentially, this is a Ramsey measurement with a π-pulse between the two $\pi/2$-pulses. The measurement is schematically depicted in figure 17. A $\pi/2$-pulse is applied (A) which takes the qubit into the xy-plane (B), where it precesses around the plane (C). After a time t a $\pi/2$-pulse is applied (D) which leads after the same time t to an echo (F). Then another $\pi/2$-pulse is applied after which the measurement is conducted. Due to the π-pulse the phases accumulated during the time intervals t where the qubit precesses freely are subtracted from each other [18]. Different times t of the two pulses which leads to an exponential decay with the characteristic time T_2.

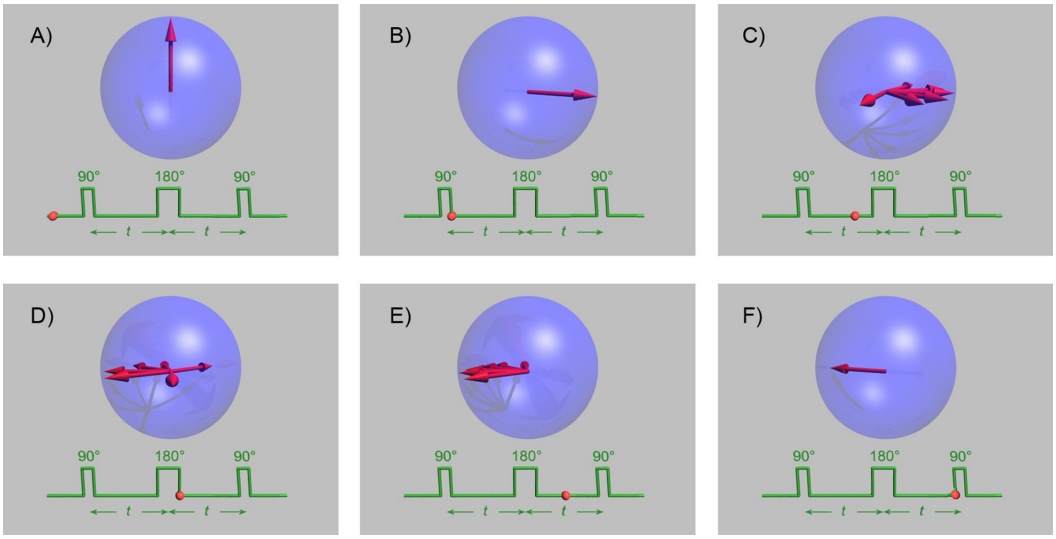

Figure 17: Measurement scheme for coherence time T_2. Modified after [19].

4.2 Measurement Setup

The measurement setup of the experiment can be divided in two sections. First, we have the dilution frigde in which the sample is placed and second, the setup for the generation of the microwave pulses to obtain different qubit lifetimes and coherence times, respectively. These setups are described in the following.

4.2.1 Dilution fridge

The cavity with the transmon chip inside was placed in the dilution fridge Bluefors 1 as depicted in figure 18. The input signal passes through three 20 dB attenuators on the

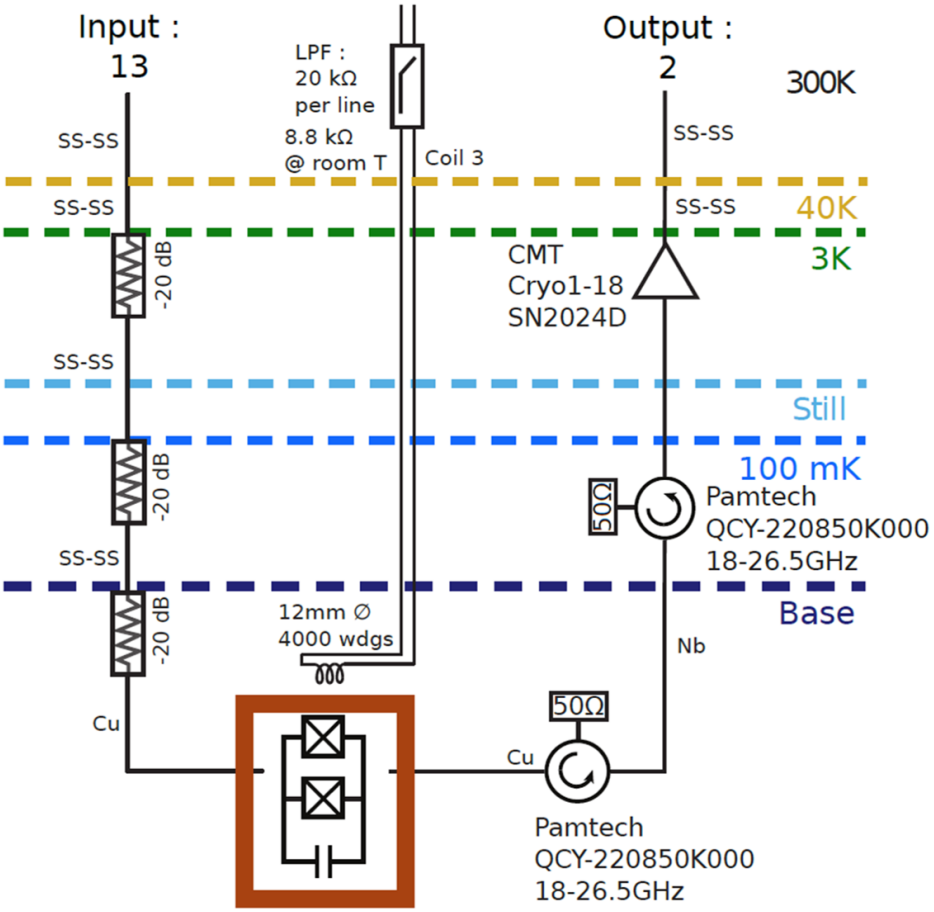

Figure 18: Dilution fridge setup. Courtesy of Sébastien Garcia.

3 K, 100 mK and base temperature level. Then it reaches the cavity which is located in the base temperature level, i.e. around ~ 10 mK. The output signal passes through two circulators and a High-Electron-Mobility-Transistor (HEMT) amplifier. Both devices are specific for the used frequency range.

A coil is attached to the cavity which allows to tune the transmon qubit transition frequency. The cavity is placed inside two magnetic shields of μ-metal to reduce magnetic fluctuations.

4.2.2 Microwave generation

A special up-conversion setup was used which is depicted in figure 19. This setup uses a In-phase and Quadrature (IQ) mixer at low frequency which generates an intermediate frequency signal at 4 GHz from the Arbitraty Waveform Generator (AWG) around 120 MHz and a Local Oscillator (LO) around 4.12 GHz. The signal passes through a low-pass filter, a DC block and a switch which allows to measure the power of the signal

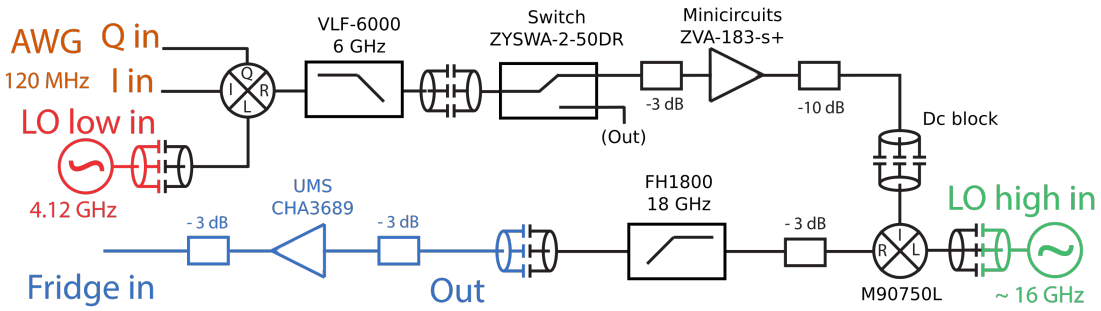

Figure 19: Up-conversion setup. Courtesy of Sébastien Garcia.

or passing further. In the latter case, the signal passes through some attenuators and is amplified. After another DC-block the signal is multiplied in by a three-port-mixer with another LO around 16 GHz. Through the subsequent high-pass filter, the carrier and the sideband frequency at 16 GHz and 12 GHz, respectively, are strongly suppressed. After another DC-block, some more attenuators and an amplifier, the signal is finally reaches the input line of the dilution fridge.

The down-conversion of the output signal used in the experiment is depicted in figure 20. The signal passes through some amplifiers and attenuators as well as a high and low pass filter. Then a three-port-mixer is used with a LO to downconvert the output frequency. Then the signal is further attenuated, amplified and passes some low-pass filters. Finally, the signal is detected by a Field Programmable Gate Array (FPGA).

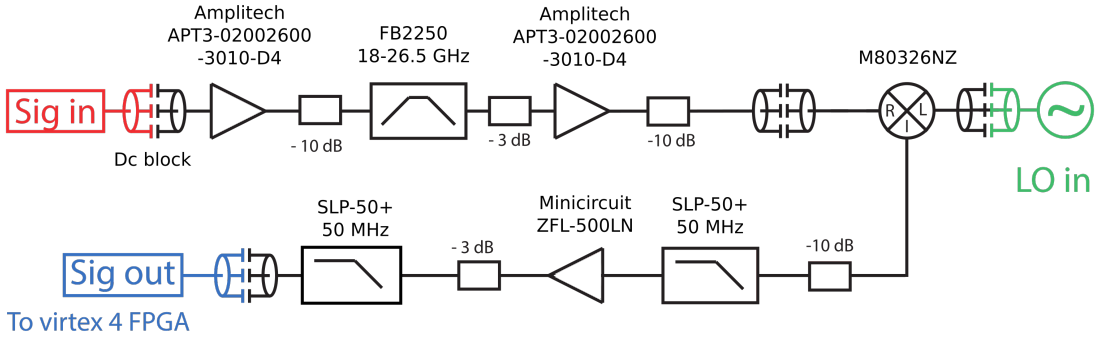

Figure 20: Down-conversion setup. Courtesy of Sébastien Garcia.

5 Results

This section presents the results obtained during the measurements of the cavity-qubit system in the dilution fridge. First, the obtained data close to resonance of the system is shown which allows to extract the basic parameters of the system. Then the qubit lifetimes that were introduced in section 4.1 are presented and discussed.

5.1 Tuning the qubit frequency around resonance

As a first step, two-tone spectroscopy and measurements of the cavity transmission around its resonant frequency are conducted. A two-tone spectroscopy gives two frequencies as an input, namely the resonant frequency of the cavity and a second frequency which is scanned over a frequency range, and measures the response of the cavity-qubit system. The combined result of these two measurements is depicted in figure 21a. The

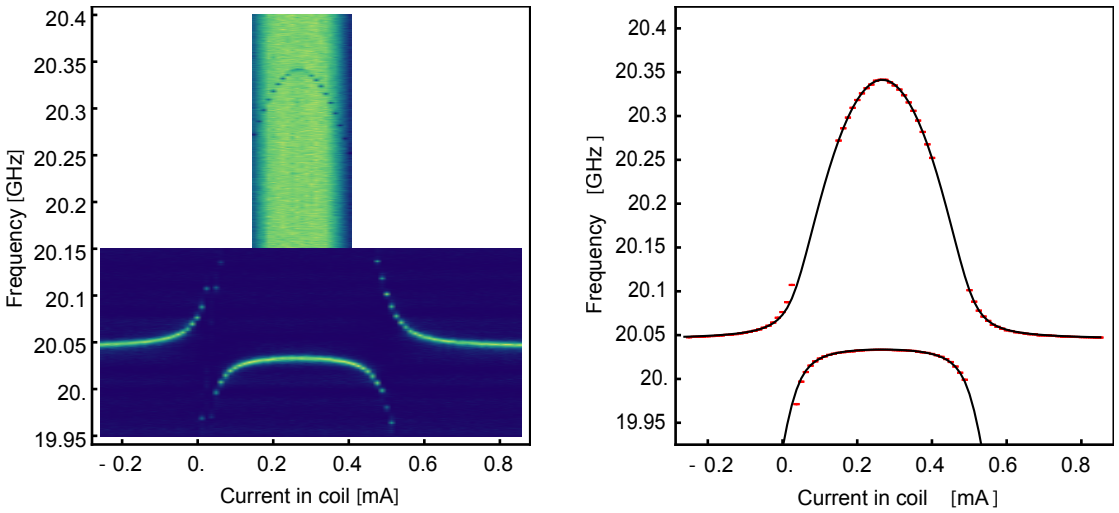

(a) (b)

Figure 21: (a) Combined two-tone spectroscopy (lower part) and transmission measurement of the cavity (upper part) around the resonant frequencies. (b) Measurement fit (in red) and the theoretical model (in black) adjusted manually as described in the text.

graph is roughly centered around the sweet spot and shows the typical anti-crossing when the qubit is resonant with the cavity. Each of the different measurements is fitted as can be seen in red in figure 21b. In solid black the theoretical spectrum of the cavity-qubit system is shown which has been adjusted manually, leading to the following parameters of the system.

The eigenfrequency of the cavity is found to be at $f_{\text{cav}} \simeq 20.0453$ GHz which is slightly lower than the one that was measured at room temperature, where the inside of the cavity was filled with air rather than vacuum, but slightly higher than the eigenfrequency

predicted by the simulation. The current offset is given by 0.267 mA and the current period is found to by 3.123 mA.

A two-tone measurement with the qubit largely detuned from the cavity ($\Delta \gg g$) can be used to estimate the charging energy. This can be obtained by two-tone measurement of the qubit transition frequency between the ground and excited state f_{ge} and the 2-photon transition between the ground and the second excited state $f_{gf}/2$. Using equation 13, we know that $f_{ef} = f_{ge} - E_C/h$ and thus $E_C/h = (f_{ge} - f_{gf}/2) \cdot 2 \simeq$ 732 MHz. This value is quite far away from the designed value of $E_C/h = 928$ MHz. A possible explanation could be that the junction surface capacitance is actually larger that the 60 fF/μm^2 assumed. Taking the capacitances of the produced transmon into account, we find the junction surface capacitance to be 82.8 fF/μm^2. This value is higher than the normal values around $50 - 75$ fF/μm^2 as stated in [20]. It is also possible that the capacitances are different because probing the sample may cause damages on the surface which can lead to different geometric capacitances.

The maximal qubit frequency is found to be $f_q \simeq 20.341$ GHz. The qubit, however, was designed for a maximal frequency of 24 GHz. The reduced frequency can be explained by the fact that the charging energy as well as the Josephson energy are lower than originally expected from the design.

The maximal Josephson energy can be computed using equation 13 once we know the charging energy and the maximal qubit frequency which leads to $E_J/h \simeq 75.8$ GHz, which is the same value as for the manual adjustment of the theoretical model. The designed value with $E_J/h \simeq 83.7$ GHz is higher. A possible explanation is that the assumed normal resistance per area of $R_{n,A_J} \simeq 200$ $\Omega.\mu$m^2 is different in our production process. Considering the measured value of the Josephson energy, we expect $R_{n,A_J} \simeq$ 221 $\Omega.\mu$m^2.

The coupling constant can be estimated by a measurement where the cavity and qubit are close to resonant, see figure 22a. In the manual adjustment of the theoretical model, the coupling constant is found to be $g/2\pi \simeq 59$ MHz. This value is slightly different from the one expected from our design with $g/2\pi \simeq 70$ MHz. The remaining discrepancy could be from the fact that we probe the transmon and therefore, damages can occur which have an effect on the coupling constant.

The data from spectroscopy conducted in figure 21 can be further processed by fitting the line widths of the cavity-like mode. As we can observe in figure 22b, the linewidths decrease when the qubit approaches the resonant frequency of the cavity. At resonance the cavity and qubit state are mixed which leads also to a mixing of the decays, i.e. on resonance decay of the eigenstates is given by the average of the two subsystem decays. Therefore, since the losses of the cavity are reduced at this region, we conclude that the qubit lifetime is longer than the one of cavity photons.

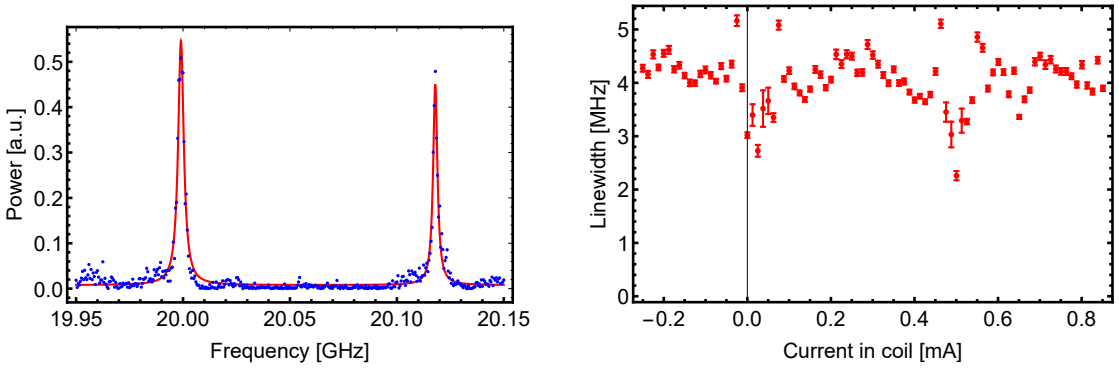

(a) (b)

Figure 22: (a) Double Lorentzian fit of the transmission spectroscopy where the qubit and the cavity a close to resonance. (b) Lorentzian fitted linewidths of the spectroscopy given in figure 21.

5.2 Time resolved measurements

The energy-relaxation and decoherence times of the qubit can be extracted by the time resolved measurements as depicted in figure 23 for the qubit with a frequency of 18.462 GHz. The measurement is conducted and analyzed with *QubitCalib* which was programmed by the group. Each of the measurements was averaged over 60,000 experiments. The measurement procedure is the following: As a first step, a Rabi measurement is conducted to find the corresponding π- and $\pi/2$- pulses. Then a first Ramsey-experiment is conducted with a detuning of ± 4 MHz of the qubit frequency in order to measure the qubit frequency more precisely. Then another Rabi measurement is conducted to extract the exact pulses needed for the subsequent lifetime measurements, i.e. first, the Ramsey measurements which yields T_2^*, then the energy relaxation time measurements that allows to extract T_1, and finally, the spin-echo measurement which allows us to conclude for T_2.

These kind of measurements were conducted for different qubit frequency. The corresponding lifetimes are depicted in figure 24. Additionaly, the Purell-limited lifetime is shown as well as a total T_1 curve that is based on the idea that we do not have only the Purcell lifetime but also an assumed intrinsic frequency-independent lifetime, i.e. $T_1 = \frac{1}{\frac{1}{T_{1,\text{Purcell}}}+\frac{1}{T_{1,\text{int}}}}$ with $T_{1,\text{int}} = (1.96 \pm 0.01)$ µs. It can be observed that all times decrease when they approach the Purcell-limited lifetime. All lifetimes are in the order of µs. The Spin-Echo time T_2 is larger than the other times, especially for lower frequencies.

Compared to the 7 GHz tunable transmon qubit in [15], the lifetimes are shorter. T_1 is about 7 times smaller, T_2^* is of similar magnitude and T_2 is about 2-3 times smaller. Interestingly, T_1 is of the same magnitude as T_2^*, whereas in [15] T_1 was exceeding T_2.

Another 20 GHz tunable transmon qubit was produced and measured previously in the lab. Here, T_1 was about two times larger than for the transmon qubit in this thesis.

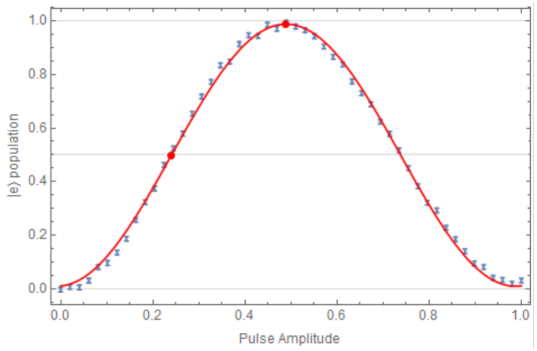

(a) Rabi measurement

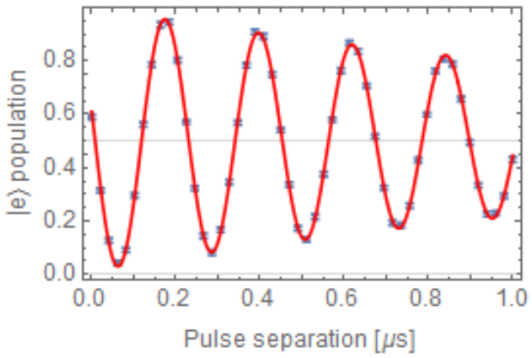

(b) Ramsey measurement

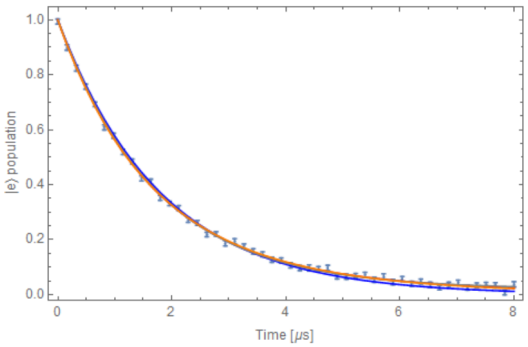

(c) T_1 measurement

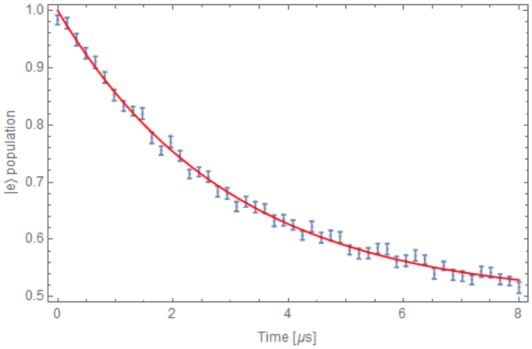

(d) T_2 measurement

Figure 23: Example measurements for the qubit lifetimes. The voltage is set to 3.4 V which corresponds to a qubit frequency of 18.462 GHz. The different measurements denote the (a) Rabi osciallation, which allows for calibration of the applied pulses, (b) the Ramsey measurement, whose envelope contains T_2^*, (c) the energy relaxation time T_1 measurement and (d) the Spin-Echo measurement which yields T_2.

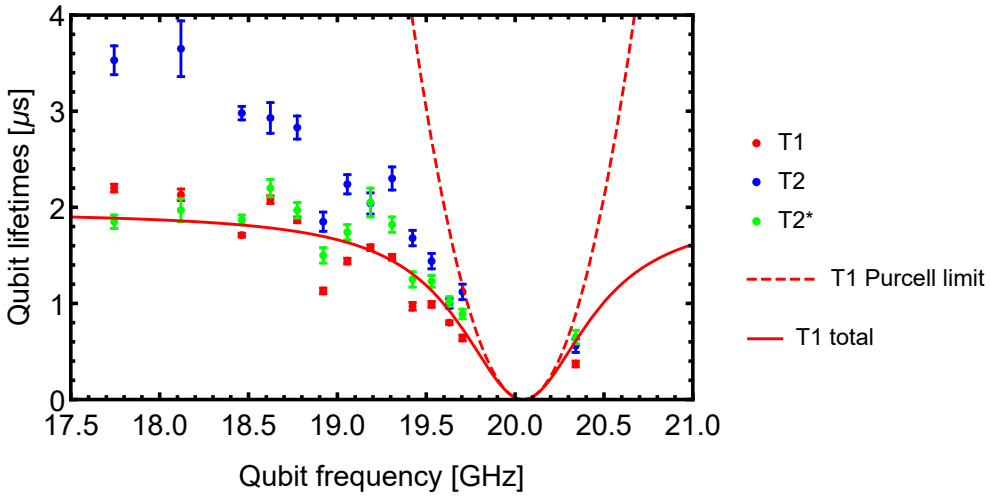

Figure 24: Energy relaxation T_1, Ramsey T_2^* and spin-echo T_2 as a function of the qubit frequency. The Purcell-limited lifetime is depicted with the dashed red line. The total time T_1 as a function of the Purcell-limited lifetime and an assumed constant lifetime, see text.

However, T_2 is of the same magnitude and T_2^* is for our design almost twice as large compared to the other 20 GHz qubit.

6 Conclusion and Outlook

The experiment has shown that the transmon properties in a 3D cavity can be extended to a frequency range around of 20 GHz. The tunability of the transmon worked like it is known from the lower frequency systems. In the spectroscopy measurements the typical properties of the qubit-cavity system were observed. Since our design predictions only matched the results to a certain degree, it would be interesting to further investigate the possible reasons for that. A better knowledge on the junction surface capacitances as well as the effect that can be caused by the SQUID loop being located not inbetween the pads would therefore be of interest.

The time resolved measurements showed that it is possible to achieve qubit lifetimes of the order of $2-4$ µs. These lifetimes are worse than the ones for the 7 GHz transmon systems, however, the Ramsey T_2^* lifetime is of the same magnitude in both cases. In order to get a better idea of how the transmon behaves at this frequency range, it could be of interest to test different transmon designs and also check the evolution of the measurement results when performing the measurements at different times.

Acknowledgement

I would like to thank Prof. Dr. Andreas Wallraff and the Qudev lab for offering me this semester project. I was able to gather thorough knowledge on quantum information processing and experience about the work with superconducting qubits and microwave resonators, microwave generation as well as detection and cryogenics systems. It was very impressive to see how many details have to be considered especially in the experimental setups.

In particular, I would like to thank my supervisor Dr. Sébastien Garcia for his guidance and help throughout this project. Thank you for your time, advice and continuous patience to find the errors and mistakes whenever something was not working as intended.

Additionally, I would like to thank Jean-Claude Besse who produced the transmon chip for our experiment and Dr. Simone Gasparinetti who lent us the measurement setup for our measurements at cryogenic temperatures. And last but not least, I would like to thank the whole group for providing many programmes, which I could use for the measurements and its evaluation, and for the always welcoming and nice atmosphere.

References

[1] M. H. Devoret, A. Wallraff, and J. M. Martinis. Superconducting qubits: A short review, `arXiv:cond-mat/0411174`. 2004.

[2] D.F. Walls and Gerard J. Milburn. CQED. In *Quantum Optics*, pages 213–229. Springer Berlin Heidelberg, Berlin, Heidelberg, 2008.

[3] A. Blais, R. Huang, A. Wallraff, S. M. Girvin, and R. J. Schoelkopf. Cavity quantum electrodynamics for superconducting electrical circuits: An architecture for quantum computation. *Phys. Rev. A*, 69:062320, Jun 2004.

[4] R. J. Schoelkopf and Girvin S. M. Wiring up quantum systems. *Nature*, 451:664–669, Feb 2008.

[5] Y. Reshitnyk, M. Jerger, and A. Fedorov. 3D microwave cavity with magnetic flux control and enhanced quality factor. *EPJ Quantum Technology*, 3(1):13, Oct 2016.

[6] H. Paik, D. I. Schuster, L. S. Bishop, G. Kirchmair, G. Catelani, A. P. Sears, B. R. Johnson, M. J. Reagor, L. Frunzio, L. I. Glazman, S. M. Girvin, M. H. Devoret, and R. J. Schoelkopf. Observation of High Coherence in Josephson Junction Qubits Measured in a Three-Dimensional Circuit QED Architecture. *Phys. Rev. Lett.*, 107:240501, Dec 2011.

[7] D. M. Pozar. *Microwave Engineering*. Wiley, 4th edition, 2011.

[8] C. W. Gardiner and M. J. Collett. Input and output in damped quantum systems: Quantum stochastic differential equations and the master equation. *Phys. Rev. A*, 31:3761–3774, Jun 1985.

[9] J. Koch, T. M. Yu, J. Gambetta, A. A. Houck, D. I. Schuster, J. Majer, A. Blais, M. H. Devoret, S. M. Girvin, and R. J. Schoelkopf. Charge-insensitive qubit design derived from the Cooper pair box. *Phys. Rev. A*, 76:042319, Oct 2007.

[10] M. Roth. *Influence of Additional Pads on the Electrical Properties of a 3D Transmon*. Semester Thesis, ETH Zurich, 2015.

[11] M. Tinkham. *Introduction to Superconductivity*. Dover Publications, Inc., 2nd edition, 1996.

[12] D. A. Steck. *Quantum and Atom Optics*. available online at `http://steck.us/teaching` (revision 0.12.2, 11 April 2018).

[13] T. Menke. *Realizing a Calibration Program for Superconducting Qubits*. Semester Thesis, ETH Zurich, 2013.

[14] R. A. Bianchetti. *Control and readout of a superconducting artificial atom*. PhD thesis, ETH Zurich, 2010.

[15] J. Fankhauser. *Frequency-tunable Transmon qubit in a 3D copper cavity.* Semester Thesis, ETH Zurich, 2016.

[16] S. Girvin. Circuit QED: superconducting qubits coupled to microwave photons. In Robert Schoelkopf Devoret, Benjamin Huard and Leticia F. Cugliandolo, editors, *Quantum Machines: Measurement and Control of Engineered Quantum Systems: Lecture Notes of the Les Houches Summer School: Volume 96, July 2011*, chapter 3, pages 113–255. Oxford University Press, 2014.

[17] H. Y. Carr and E. M. Purcell. Effects of Diffusion on Free Precession in Nuclear Magnetic Resonance Experiments. *Phys. Rev.*, 94:630–638, May 1954.

[18] D. Vion, A. Aassime, A. Cottet, P. Joyez, H. Pothier, C. Urbina, e D. Estev, and M.H. Devoret. Rabi oscillations, Ramsey fringes and spin echoes in an electrical circuit. *Fortschritte der Physik*, 51(45):462–468.

[19] G. W. Morley. `https://commons.wikimedia.org/w/index.php?curid=15380381`, last accessed on 26.03.18.

[20] S. V. Lotkhov, E. M. Tolkacheva, D. V. Balashov, M. I. Khabipov, F.-I. Buchholz, and A. B. Zorin. Low hysteretic behavior of alaloxal josephson junctions. *Applied Physics Letters*, 89(13):132115, 2006.

ETH

Eidgenössische Technische Hochschule Zürich
Swiss Federal Institute of Technology Zurich

Declaration of originality

The signed declaration of originality is a component of every semester paper, Bachelor's thesis, Master's thesis and any other degree paper undertaken during the course of studies, including the respective electronic versions.

Lecturers may also require a declaration of originality for other written papers compiled for their courses.

I hereby confirm that I am the sole author of the written work here enclosed and that I have compiled it in my own words. Parts excepted are corrections of form and content by the supervisor.

Title of work (in block letters):

A TUNABLE 20 GHZ TRANSMON QUBIT IN A 3D CAVITY

Authored by (in block letters):

For papers written by groups the names of all authors are required.

Name(s):	**First name(s):**
Miller	Stefanie

With my signature I confirm that

- I have committed none of the forms of plagiarism described in the 'Citation etiquette' information sheet.
- I have documented all methods, data and processes truthfully.
- I have not manipulated any data.
- I have mentioned all persons who were significant facilitators of the work.

I am aware that the work may be screened electronically for plagiarism.

Place, date	**Signature(s)**
26.06.2018	Stefanie Miller

For papers written by groups the names of all authors are required. Their signatures collectively guarantee the entire content of the written paper.